Journal of Alloys and Compounds 509 (2011) 281–289

Contents lists available at ScienceDirect

Journal of Alloys and Compounds

journal homepage: www.elsevier.com/locate/jallcom

TEM characterization of pure and transition metal enhanced $NaAlH_4$

Per Erik Vullum[a,*], Mark P. Pitt[b], John C. Walmsley[a,c], Bjørn C. Hauback[b], Randi Holmestad[a]

[a] Department of Physics, Norwegian University of Science and Technology (NTNU), Høgskoleringen 5, 7491 Trondheim, Norway
[b] Institute for Energy Technology, P.O. Box 40, NO-2027 Kjeller, Norway
[c] SINTEF Materials and Chemistry, Høgskoleringen 5, 7465 Trondheim, Norway

ARTICLE INFO

Article history:
Received 15 June 2010
Received in revised form 23 August 2010
Accepted 25 August 2010
Available online 9 September 2010

Keywords:
Metal hydrides
Alanates
TEM

ABSTRACT

Possibilities and limitations in using transmission electron microscopy to characterize pure $NaAlH_4$ and transition metal enhanced $NaAlH_4$ have been investigated in detail. $NaAlH_4$ is extremely sensitive to O_2 and H_2O and must be handled under inert atmosphere at all times. Furthermore, it is highly unstable under the electron beam and only basic techniques such as diffraction contrast imaging and selected area diffraction that can be performed with a low flux electron beam can be used without the $NaAlH_4$ decomposing. By comparison, phases containing transition metal additive are very stable under the electron beam. The latter are investigated by a combination of high resolution imaging, electron diffraction and spectroscopy to determine distribution, composition, crystal structure and defect content in ball milled and hydrogen cycled, $TiCl_3$ and $FeCl_3$ enhanced $NaAlH_4$. It is demonstrated that a large amount of the added Ti or Fe is located at the surface of the $NaAlH_4$ grains as a combination of crystalline and amorphous $Al_{1-x}TM_x$ (TM = Ti, Fe) nanoparticles.

© 2010 Elsevier B.V. All rights reserved.

1. Introduction

A reliable method for reversible hydrogen storage is the key requirement for onboard use of hydrogen in transportation applications. Among the various approaches for hydrogen storage, complex hydrides are seen to be one of the most promising group of materials [1]. Pure complex hydrides are not considered as viable candidates for reversible hydrogen storage due to the high stability of the materials at operating conditions for fuel cells, and lack of H reversibility. However, in 1997 Bogdanovic and Schwickardi discovered that adding transition metals, such as Ti, to $NaAlH_4$ enabled reversible hydrogen absorption at moderate temperatures [2]. In addition, the kinetics of hydrogen reabsorption increased by several orders of magnitude. A theoretical storage capacity of about 5.5 wt.% H_2 can be reversibly released in a two step decomposition forming NaH and Al as the final products:

$$3NaAlH_4 \leftrightarrow Na_3AlH_6 + 2Al + 3H_2(3.7\,wt.\%) \quad (1)$$

$$Na_3AlH_6 \leftrightarrow 3NaH + Al + 1.5H_2(1.8\,wt.\%) \quad (2)$$

Since the discovery of adding Ti to $NaAlH_4$, numerous research groups have tried to optimize the parameters involved in reversible hydrogen storage with respect to kinetics and storage capacity. However, further optimization depends on a thorough understanding of one fundamental question: what are the state, location and role of the added Ti during reversible hydrogen storage in $NaAlH_4$? The efforts made to solve this question span over a wide range of experimental techniques, including X-ray diffraction (XRD) [3–6], neutron diffraction [7], infrared (IR) and Raman spectroscopy [8], anelastic spectroscopy [9], differential scanning calorimetry (DSC) [10,11], electron paramagnetic resonance (EPR) [12], X-ray absorption spectroscopy (XAS) [13–15], X-ray photoelectron spectroscopy (XPS) [16–18], inelastic and quasielastic neutron scattering [19,20], nuclear magnetic resonance (NMR) [21,22], muon spin rotation (μSR) [23], scanning electron microscopy (SEM) [3,18,24], and transmission electron microscopy (TEM) [24–29]. In addition, numerous density functional theory (DFT) calculations have studied possible Ti substitution scenarios in the bulk and at the surface of $NaAlH_4$ [30–38].

While interest has expanded to further complex hydride systems, it is clear that the fundamental principles of the hydrogen storage behavior of these materials are still not fully understood, particularly the role of added transition metal. In this context, the $NaAlH_4$ system retains a fundamental interest as it is the most extensively studied, possessing only moderate stability.

Despite the massive amount of work put into the understanding of the catalytic effects of Ti, only a few conclusions have been drawn. It has been verified, both theoretically [30] and experimentally [5], that bulk substitution of Ti into $NaAlH_4$ is very unlikely. It is also clear, based on EPR [12], XPS [30] and XAS [15,26,39], that Ti is largely reduced to a metallic, zero-valent state during ball milling. However, any Ti containing phase is invisible to most experimen-

* Corresponding author. Tel.: +47 93016522; fax: +47 73597710.
E-mail addresses: Per.Erik.Vullum@sintef.no, per.vullum@ntnu.no (P.E. Vullum), mark.pitt@gmail.com (M.P. Pitt), John.Walmsley@sintef.no (J.C. Walmsley), Bjorn.Hauback@ife.no (B.C. Hauback), randi.holmestad@ntnu.no (R. Holmestad).

0925-8388/$ – see front matter © 2010 Elsevier B.V. All rights reserved.
doi:10.1016/j.jallcom.2010.08.149

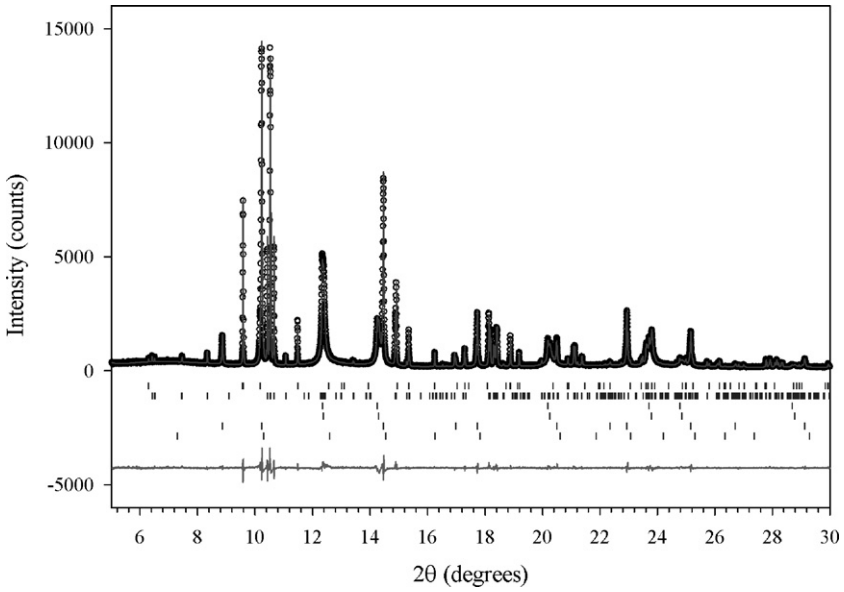

Fig. 1. High resolution X-ray synchrotron diffraction pattern of $NaAlH_4 + 0.1TiCl_3$ after two hydrogen cycles. Circles show the raw data, with the solid line showing the Rietveld model calculation. The difference profile below the pattern shows the fit quality. Reflection markers from top to bottom show $NaAlH_4$, Na_3AlH_6, Al, $Al_{85}Ti_{15}$, NaCl and Al_3Ti. Quantitative proportions of each phase are given in Section 2.

tal techniques. A few X-ray diffraction studies [5,6,40–42] show a shoulder on the high angle side of the Al reflections, which has been ascribed to the presence of crystalline Al_3Ti or $Al_{1-x}Ti_x$ phases, although these $Al_{1-x}Ti_x$ phases were not able to account for all of the added Ti. Besides metallic Ti and $TiCl_3$ additives, recent work has shown the direct addition of nanoparticles of TiO_2 (10 nm × 40 nm) [43], TiN (6 nm) [44], TiB_2 (15–60 nm) [44], and microscopic TiC [45] to $NaAlH_4$ results in absorption/desorption kinetics at least as rapid as $TiCl_3$ additives. It is also observed by X-ray diffraction [43–45] that no interaction of these stable Ti containing phases occurs with $NaAlH_4$, implying that the $NaAlH_4$/Ti containing phase interface is the local structure of most interest in understanding the role of Ti based additives in producing hydrogen reversible $NaAlH_4$. The local morphology of how these additives are embedded in the surface of the $NaAlH_4$ grains is of fundamental interest, and the use of reliable and informative techniques to study these surface morphologies has been limited.

TEM is maybe the most versatile tool to characterize materials at the nanoscale. Phases and their crystal structures, interfaces and chemical compositions can potentially be analyzed down to the atomic scale. However, two problems have limited the use of TEM in the study of alanates, such as $NaAlH_4$: (a) $NaAlH_4$ is highly unstable under the electron beam, and (b) it is a challenge to transport $NaAlH_4$ into the microscope without exposing the sample to O_2 or H_2O. In this work, the possibilities and limitations by using TEM to characterize $NaAlH_4$ and Ti and Fe enhanced $NaAlH_4$ are carefully described. Moreover, it is shown how composition, crystal structure and defects of the TM phases can be determined in detail by a combination of several TEM techniques. While contributing to the fundamental understanding of the $NaAlH_4$–TM systems, the methodology described is expected to be relevant to studies of other hydrogen storage candidate materials and other air-sensitive systems. Understanding the role of the TM is a potential key to destabilizing higher wt.% and more stable hydrogen materials, such as for example $LiBH_4$ with a theoretical H storage capacity of 18.5 wt.%.

2. Experimental

$NaAlH_4$ was purchased from Albermarle Corporation (LOT NO. #:22470404-01, >93% purity), and $TiCl_3$ and $FeCl_3$ were purchased from Sigma–Aldrich Chemicals Inc. (>99.99% purities). The powders were always handled under inert atmosphere in a dry Ar glove box. $NaAlH_4$ powders, pure or mixed with $TiCl_3$ or $FeCl_3$, were prepared in 1 g quantities in a Fritsch P7 planetary mill, with ball to powder ratio of 20:1, and milled at 750 rpm for a period of 1 h. Hydrogen cycled powders (typically 140 °C/150 bar aliquot) were prepared in a Sieverts apparatus rated to 200 bar and 600 °C. Powders were removed after 2 or 5 H cycles for $TiCl_3$ and after 2 H cycles for $FeCl_3$ additives. All the studied materials were tetra hydrides, i.e. all materials loaded into the microscope were fully charged with hydrogen, being on the left side in Eq. (1). Powder X-ray diffraction data were recorded at the Swiss–Norwegian Beamline (SNBL) at the European Synchrotron Radiation Facility (ESRF) in Grenoble, France. Samples were contained in rotating 0.8 mm boron–silica glass capillaries. High resolution data ($\Delta d/d \sim 3 \times 10^{-4}$) were typically collected at 295 K between 5 and 35° 2θ, in steps of 0.003–0.030°, depending on the sample broadening. A wavelength of 0.4998 Å was obtained from a channel cut Si(1 1 1) monochromator. Typical X-ray synchrotron diffraction data of $NaAlH_4 + 0.1TiCl_3$ after two hydrogen cycles is shown in Fig. 1. Quantitative phase analysis yields phase mol fractions as $NaAlH_4$:Na_3AlH_6:Al:NaCl:$Al_{85}Ti_{15}$:Al_3Ti = 8.5%:16.8%:7.5%:25.0%:40.1%:2.1%. These phase mol fractions are consistent with those reported in [40] for $NaAlH_4 + 0.1TiCl_3$ after three hydrogen cycles. These phase proportions represent the exact state of the sample prior to TEM measurements.

Transmission electron microscopy was performed using a JEOL 2010F field emission microscope operating at 200 kV, or a Philips CM30 operating at 100–300 kV. All TEM samples were dispersed on thin, holey carbon film coated Cu grids inside the glove box and transferred into the column of the microscope by two different methods: (a) an oxygen tight transfer cover was used, with the cover being removed inside a glove bag attached to the holder entrance of the microscope. The glove bag was flushed with Ar (>99.999% purity) to prevent sample oxidation. (b) A Gatan environmental cell TEM holder was used. A vacuum gate valve on the environmental chamber allowed the sample to be withdrawn and isolated in the chamber during transfer, which prevented contamination or contact with air. The cell was evacuated by a turbomolecular-pump before being opened to the TEM vacuum. Electron diffraction patterns were integrated using the ProcessDiffraction V_4.2.4 B software package [46]. The inelastic background in the integrated diffraction patterns was subtracted by a combination of a four parameters exponential decay function and a third order polynomial.

3. Results and discussion

3.1. Decomposition and oxidation

$NaAlH_4$ is highly unstable under the electron beam, and this is clearly demonstrated by Fig. 2a–d. Fig. 2a shows an agglomerate of pure $NaAlH_4$ single crystals. These agglomerates decompose completely on a time scale of less than 5–30 s under a normal electron flux, 200 keV electron beam. The decomposition time depends on sample thickness, and on thicker sample areas it takes longer time

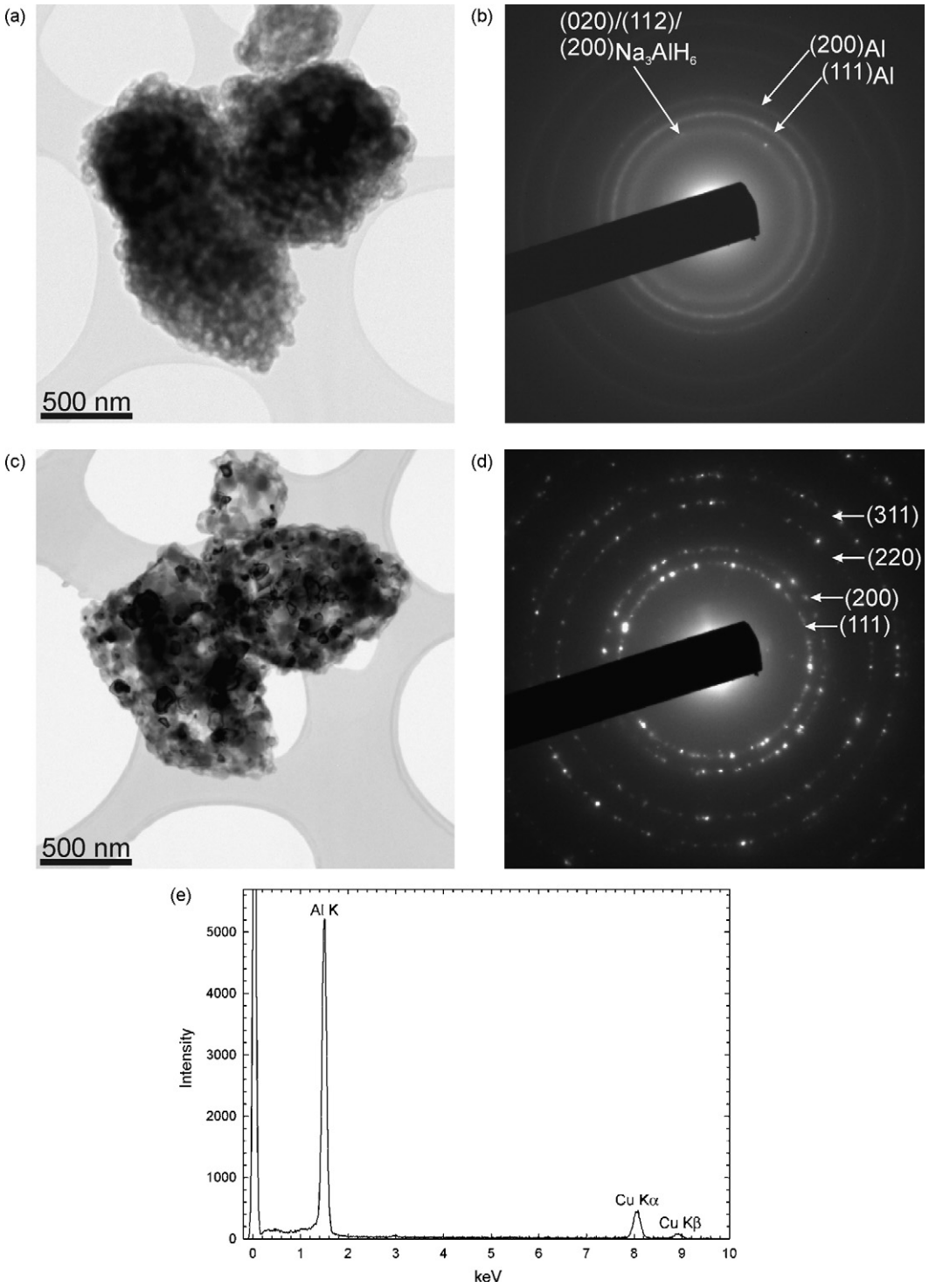

Fig. 2. (a) An agglomerate of pure $NaAlH_4$ single crystals. (b) Diffraction pattern during electron beam induced decomposition, showing nucleation of both Na_3AlH_6 and pure Al. (c) The same agglomerate as (a), but after decomposition under the electron beam. The final product is small, ca. 40 nm crystallites of face centered cubic Al crystallites. (d) The diffraction pattern corresponding to (c), showing only semi-continuous diffraction rings from Al. (e) The EDS spectrum from the decomposition product shown in (c). Al is the only element present in the spectrum, in addition to the Cu peaks due to the Cu grid and the environment around the sample and detector.

than on thin areas to complete the decomposition. A diffraction pattern recorded at the very beginning of the decomposition is shown in Fig. 2b. This pattern is characterized by rings with almost homogeneous, continuous intensity, rather than discrete spots. The inner ring is located at 2.70–2.75 Å. Using the crystal structure data of α-Na_3AlH_6 given by Rönnebro et al. [47], the strong (0 2 0), (1 1 2) and (2 0 0) diffraction lines should be found at 2.76 Å, 2.73 Å and 2.70 Å, respectively. In a typical low resolution electron diffraction pattern, these reflections form a single broad band of intensity. The remaining, sharper rings are due to metallic Al. Further growth of Na_3AlH_6 nuclei, as would be expected during the hydrogen cycling process defined in Eq. (1), is bypassed by the evaporation of Na and H and nucleation and growth of pure Al. From a thermodynamic point of view, NaH is the most stable hydride of those involved in the hydrogen cycling process. However, a possible nucleation and growth of NaH never occurs as both Na and H evaporate too rapidly from the

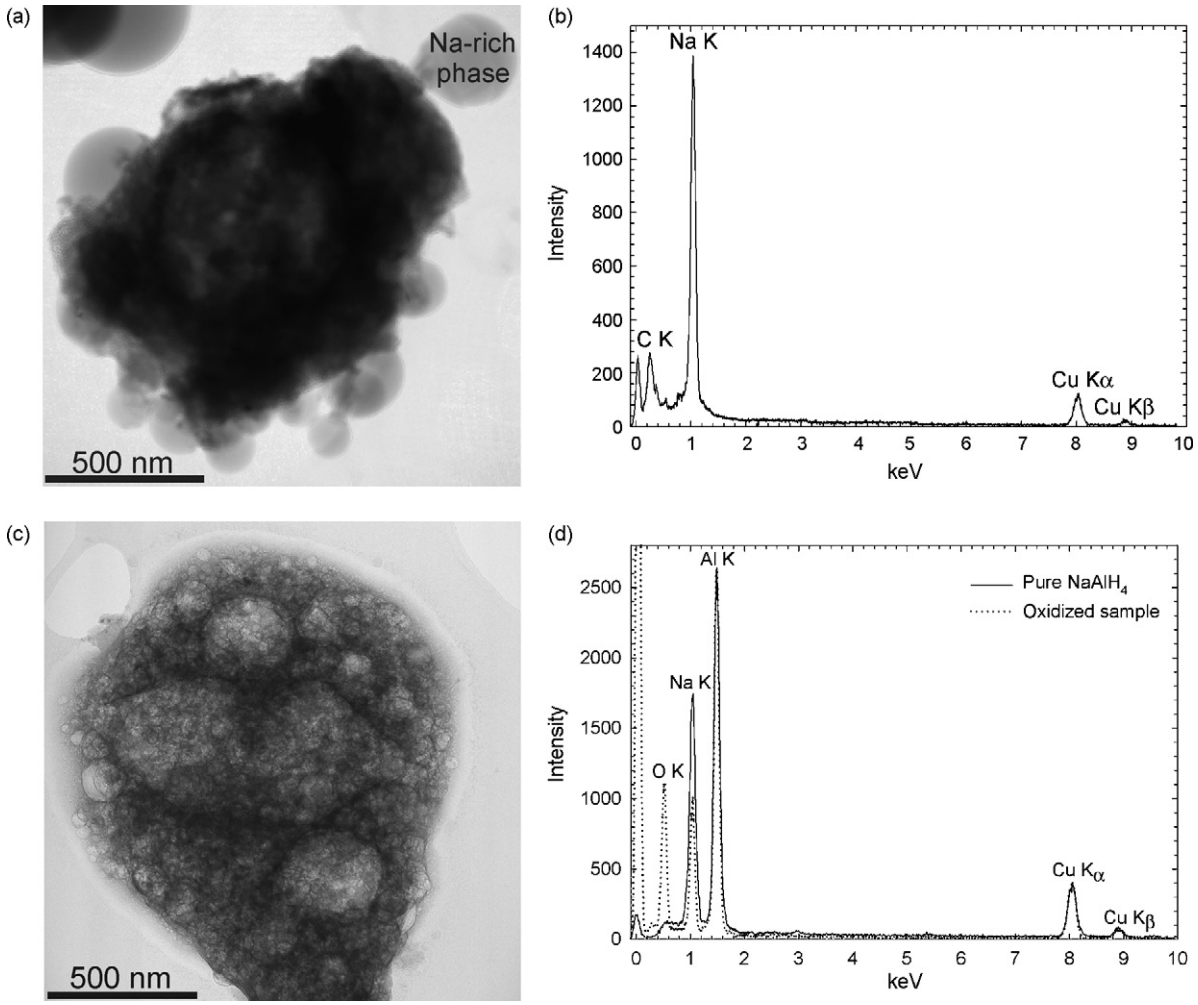

Fig. 3. (a) $NaAlH_4$ agglomerate with Na-rich particles growing at the surface of $NaAlH_4$ grains due to electron beam decomposition. (b) The Na-rich composition of these surface particles is demonstrated in the EDS spectrum from such a particle. (c) Example of an oxidized $NaAlH_4$ particle with different morphology and structure compared to the pure $NaAlH_4$ agglomerate in Fig. 2(a). (d) EDS spectrum from a pure $NaAlH_4$ agglomerate (solid line), similar to the one shown in Fig. 2(a), and a second spectrum from an oxidized particle (dotted line), similar to the oxidized particle in (b). The two spectra are normalized with respect to the Al K peak.

sample under the electron beam. The final decomposition product of the aggregate is shown in the bright field image in Fig. 2c. Morphology, crystal structure and composition have changed during the decomposition. Electron dispersive spectroscopy (EDS) (which is insensitive to H) from the decomposition product is shown in Fig. 2e. Except for the Cu peaks due to the Cu grid and the environment around the sample and detector, only Al is present in the spectrum. The diffraction pattern from the decomposition product is shown in Fig. 2d. Diffraction from face centered cubic Al is the only Bragg scattered intensity present. Based on the combination of EDS and diffraction, one can conclude that all of the Na and H have evaporated during decomposition, and the product is an agglomerate of Al crystallites with an average size of ca. 40 nm. Similar results were reported as early as 1983 by Herley and Jones [48], on a pure $NaAlH_4$ single crystal. Fig. 3a shows a bright field image at the beginning of the decomposition process. This image was acquired from a different agglomerate than that shown in Fig. 2, but gives additional information to the decomposition process. Non-crystalline, spherical particles grow at the surface of the $NaAlH_4$ crystals and evaporate from the agglomerate during decomposition. In Fig. 3b, only Na is seen in the EDS spectrum from these surface particles (except for C due to the holey carbon film and the before mentioned Cu peaks), they display homogeneous image contrast without any diffraction, suggesting a non-crystalline character.

In an attempt to avoid rapid $NaAlH_4$ decomposition, the electron beam energy was reduced from 200 to 100 keV, and the sample was cooled with liquid nitrogen. Very minor reduction of the decomposition rate was achieved under these conditions, demonstrating that the main cause of the decomposition is “knock on” damage rather than heating. The use of a very low electron flux was the only effective way to preserve the $NaAlH_4$.

Aside from the problem of decomposition under the electron beam, oxidation during sample handling and transfer is a challenge that must be addressed. An oxidized $NaAlH_4$ particle is shown in Fig. 3c. The morphology and crystal structure of this particle is very different from the pure $NaAlH_4$ agglomerate shown in Fig. 2a, and the stability under the electron beam is very good, in strong contrast with the alanate phases. Most of the Al and Na are bound in the form of stable oxides. No decomposition could be observed when focusing the beam onto the particle and EDS showed an average composition with more than 50 at.% of O, compared to small, almost negligible O values when measured on particles such as the $NaAlH_4$ agglomerate shown in Fig. 2a. The low (typically close to the detection limit of EDS) O content found in samples such as the agglomerate in Fig. 2, appears to be negligible. However, even the smallest amounts of O in the form of surface oxides might affect both the storage capacity and the kinetics during hydrogen cycling. Typical EDS spectra from oxidized and non-oxidized $NaAlH_4$ parti-

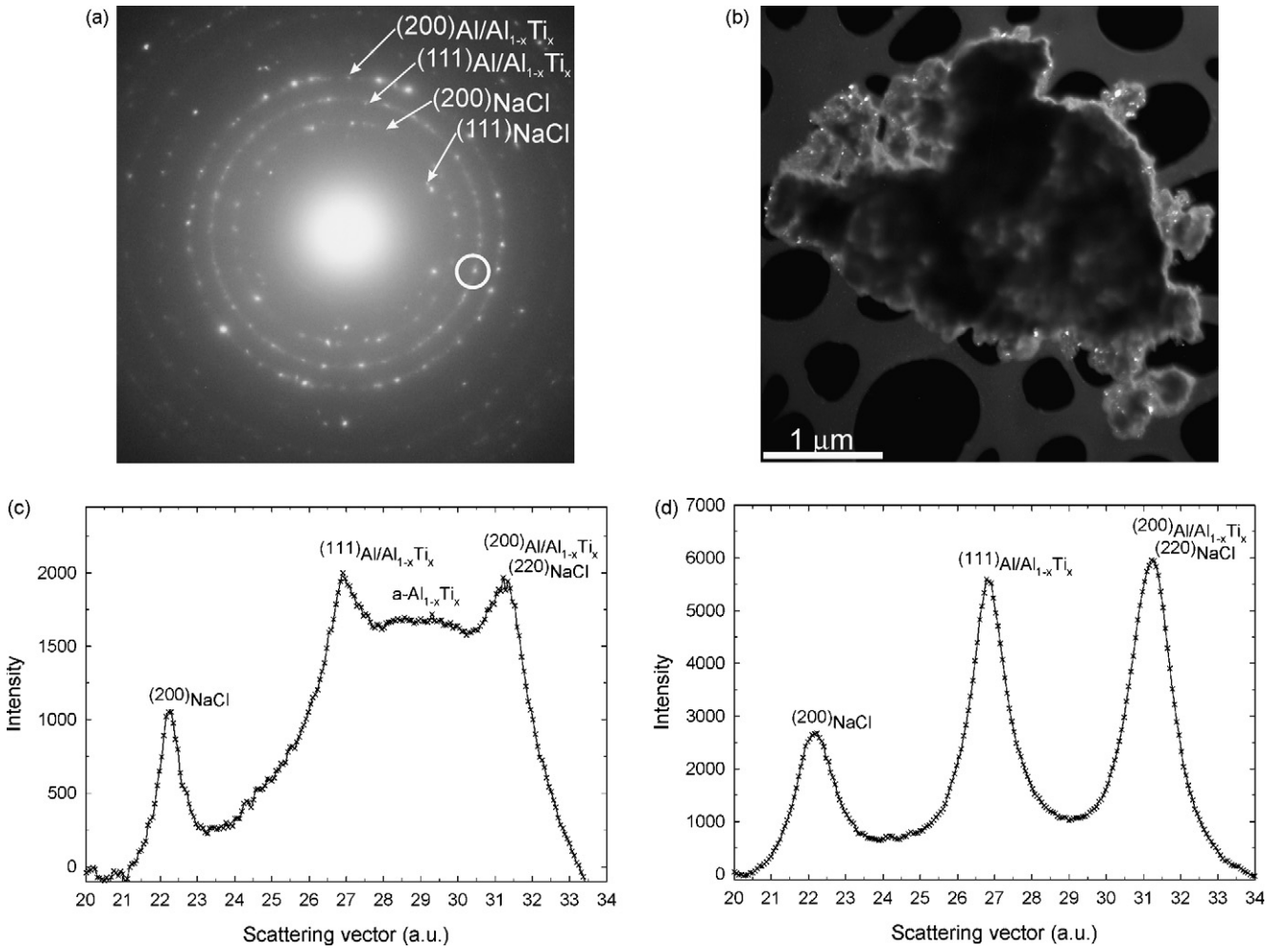

Fig. 4. (a) Diffraction pattern from a particle in $NaAlH_4$ + 0.1$TiCl_3$. (b) Dark field image of an agglomerate of grains. The dark field image was made with the Bragg scattered $Al_{1-x}Ti_x$ diffraction spots inside the circular area marked on the diffraction pattern in (a). (c) Integrated diffraction patterns which shows that some areas have amorphous $Al_{1-x}Ti_x$ in addition to crystalline $Al_{1-x}Ti_x$. (d) In some parts of the material, Ti exists only in the form of crystalline $Al_{1-x}Ti_x$ ($x < 0.25$).

cles are shown in Fig. 3d. The particle shown in Fig. 3c was never exposed directly to air, and the oxidation occurred due to storage and preparation in a contaminated glove box with O_2 content in the range 20–50 ppm. Comparison of Figs. 2a and 3c demonstrates the importance of careful sample handling without any exposure to air. Several previous TEM characterizations of alanate systems, such as Refs. [24,27], are therefore of little value since both morphology and O concentrations shown in these references are comparable to the oxidized particle shown in Fig. 3c. TEM imaging and elemental mapping will therefore give information about the oxidation products rather than the unmodified $NaAlH_4$ system.

The high oxygen sensitivity of $NaAlH_4$ means that all samples must be stored and handled under conditions similar or better than those inside an argon glove box with O_2 and H_2O contents of <1 ppm. Most frequently, a mobile glove bag was attached to the microscope during sample transfer, method (a) as described in Section 2. Even though this glove bag was emptied and flushed three times with Ar before removing the sample cover, one might still expect a higher oxygen partial pressure inside the glove bag compared to the glove box. Method (b) the environmental cell sample holder was also used to transfer samples. The latter technique guarantees that the sample is only exposed to the glove box atmosphere or vacuum before examination. However, no difference in sample quality could be observed between the two transfer techniques. The atmosphere inside the glove bag was satisfactory to protect the sample during the few seconds used to remove the cover and load the sample into the high vacuum conditions in the column of the TEM.

$NaAlH_4$ decomposition is sometimes unavoidable and limits to a high degree which kind of TEM techniques can be used without destroying the sample. The very low electron flux required in order to preserve the sample only allows normal bright and dark field imaging and selected area diffraction (SAD) in combination with long image exposure times in the order of tens of seconds. It is an open question if sample decomposition was completely avoided when applying these techniques, or only minimized. It was possible to record diffraction patterns without contrast from Al or any intermediate decomposition product. Still, a few Al crystallites away from Bragg condition, or Na_3AlH_6 and Al nuclei beyond the detection limit, could already be present in the sample. To some degree it was also possible to perform semi-quantitative EDS composition measurements. The following TEM settings were used on the JEOL 2010F to avoid decomposition (similar changes were made when using the Philips CM30): the electron gun emission was reduced to 120 μA in combination with a small 20 μm condenser aperture and a small 2.0 nm spot size. In addition, the illumination of the 2.0 nm spot size beam was spread to further decrease the electron flux. High resolution imaging of any hydride was not possible without rapid decomposition of the sample. Scanning transmission electron microscopy (STEM) is a low electron dose technique compared to normal TEM. However, medium and high resolution STEM also gave a fast decomposition of the $NaAlH_4$. STEM together with EDS or

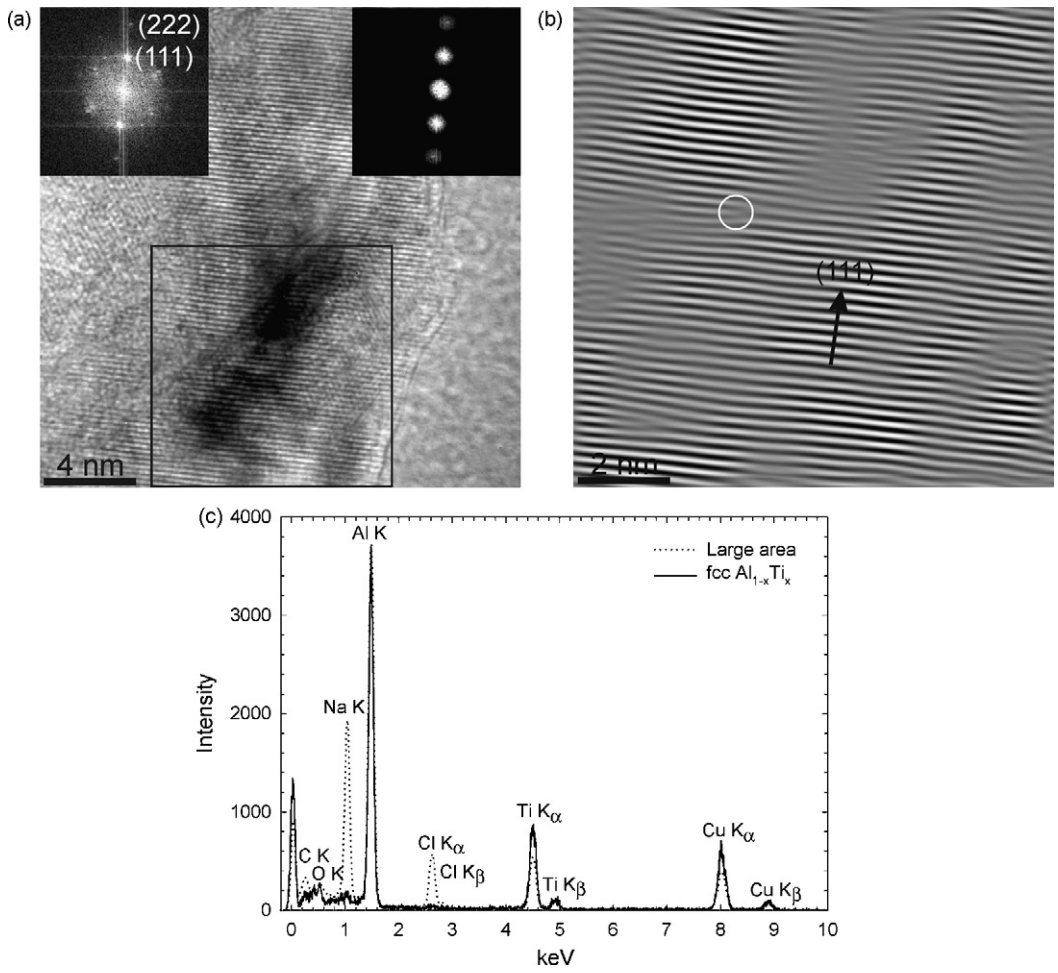

Fig. 5. (a) High resolution image of a surface embedded $Al_{1-x}Ti_x$ crystallite in ball milled and five times H cycled $NaAlH_4 + 0.1TiCl_3$. The left inset shows the Fourier transform of the area inside the square box. The right inset shows the kept part of the Fourier transform used to create the filtered high resolution image. (b) Filtered high resolution image corresponding to the area inside the square box in (a). An edge dislocation is highlighted by the circle. (c) EDS from the $Al_{1-x}Ti_x$ crystallite in (a) (solid line) compared with a spectrum (dotted line) from a larger, average part of the sample. The two spectra are normalized with respect to the Al K edge.

electron energy loss spectroscopy (EELS) can give two-dimensional elemental maps with resolution down to the sub-nanometer length scale. Even though such maps are projections convoluted with the sample thickness, valuable information about the state and location of the added transition metal could have been extracted if they could have been acquired. However, all efforts to reduce the electron flux in STEM were insufficient to prevent sample decomposition. Several authors have presented elemental maps either by the use of EDS [24,25,27] or EELS [49]. Again, it should be made clear that these maps either give information about the decomposed products or about oxides due to a partly oxidized sample.

3.2. The state and location of the added TM

So far we have considered pure $NaAlH_4$. X-ray diffraction gives the average diffraction intensity from a macroscopic sample. In the case of $NaAlH_4 + 0.1TiCl_3$, the diffractogram is a superposition of several phases. Diffraction lines from minor Ti phases are therefore difficult to deconvolute from other, more intense lines and can be difficult to detect above the background signal. TEM offers the advantage that diffraction analysis can be obtained from specific, nanoscale areas. Electron diffraction patterns can be compared with the corresponding bright or dark field images, and combined with EDS or EELS analysis. The diffraction pattern in Fig. 4a demonstrates the situation in ball milled and twice H cycled $NaAlH_4 + 0.1TiCl_3$. Diffraction from a large number of $Al_{1-x}Ti_x$ crystals is dominant in the pattern. The dark field image in Fig. 4b is made with the scattered intensity that falls inside the circular area marked in the diffraction pattern in Fig. 4a. This scattered intensity comes mainly from $Al_{1-x}Ti_x$ ($x < 0.25$), but also from pure Al [42]. Most of the small crystallites that show bright contrast in the dark field image are $Al_{1-x}Ti_x$, but some are Al. The great advantage by TEM compared to X-rays is that the diffraction signal can be correlated with a real space image of the scattering object to determine morphology and location. Moreover, EDS can be used to determine whether a specific crystallite is $Al_{1-x}Ti_x$ or pure Al. The dark field image in Fig. 4b clearly shows that many of the $Al_{1-x}Ti_x$ crystallites are located at the surface of the $NaAlH_4$ grains. However, the sample is too thick away from the edges of the agglomerate to give any contrast, and many $Al_{1-x}Ti_x$ crystallites show contrast away from the projected edge of the particle agglomerate in the thin areas. Since the image is a projection parallel to the electron beam direction, one cannot easily distinguish whether the crystallites which show contrast away from the projected edge are embedded in the $NaAlH_4$ bulk or dispersed on the $NaAlH_4$ surface. Furthermore, more detailed examination of the agglomerate requires higher electron doses and will start $NaAlH_4$ decomposition, meaning that the exact location of the Ti containing phases with respect to the $NaAlH_4$ is lost. In order to determine if all of the added Ti is located at the $NaAlH_4$ surface, or if some of the Ti is also embedded inside the $NaAlH_4$ bulk, a combinatory technique using TEM in combination with X-ray synchrotron diffraction can be used. The $NaAlH_4$ grain sizes can be

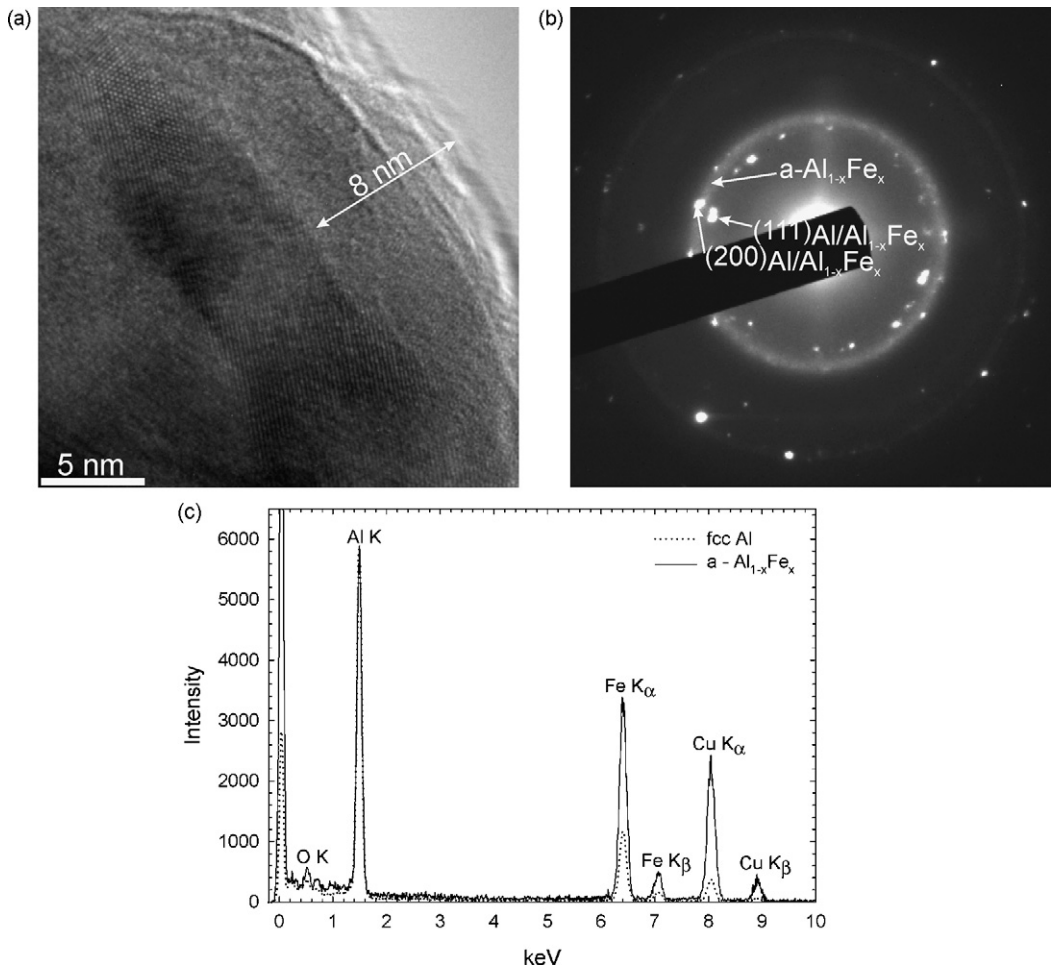

Fig. 6. (a) High resolution image from a ball milled and twice H cycled $NaAlH_4$ + 0.1$FeCl_3$ sample. A small crystallite of Al (or $Al_{1-x}Fe_x$) is embedded in an amorphous matrix of $Al_{1-x}Fe_x$ at the outer surface of a $NaAlH_4$ crystal. (b) A strong, primary amorphous $Al_{1-x}Fe_x$ halo is evident in the diffraction pattern. (c) X-ray energy dispersive spectra acquired from the amorphous region (solid line) and a crystalline region (dotted line). The two spectra are normalized with respect to the Al K peak.

extracted from the synchrotron line shapes and compared with the external grain sizes measured from TEM. A perfect match between the grain sizes found by the two techniques means that the individual particles as measured by TEM are indeed pure $NaAlH_4$ single crystals. However, if the X-ray coherence length gives a smaller grain size than the average external particle size, as measured by TEM, this implies the presence of a grain boundary network or the presence of secondary phases embedded in the $NaAlH_4$ bulk.

In an X-ray diffraction pattern with high 2θ resolution the primary amorphous halo, centered around 2.21 Å [42,50] for $Al_{1-x}Ti_x$ ($x < 0.25$), becomes very broad. In addition, diffraction lines from other phases are superimposed on the halo. Hence, the small amorphous fraction of $Al_{1-x}Ti_x$ present in $TiCl_3$ enhanced $NaAlH_4$ is practically impossible to detect with an ordinary laboratory X-ray source, and still extremely difficult to detect with a high signal to noise synchrotron source. However, with TEM one can collect diffraction patterns from highly localized areas. The two integrated diffraction patterns in Fig. 4c and d were acquired from about 100 nm in diameter areas close to the edge of a $NaAlH_4$ crystal. No amorphous halo could be observed directly in either of the two original, two-dimensional diffraction patterns. However, integration of the patterns clearly shows the primary amorphous halo between the $Al_{1-x}Ti_x$/Al (2 0 0) and (1 1 1) Bragg reflections in pattern 3c. The integrated pattern in Fig. 4d was acquired from a different part of the sample and does not show the same amorphous intensity.

Even though $NaAlH_4$ decomposes under a moderate electron flux, it should be emphasized that the various Ti (or TM) containing phases are completely stable under the electron beam. The $Al_{1-x}Ti_x$ phases can therefore be investigated in detail by high resolution techniques, and EDS or EELS can verify that a crystallite is really $Al_{1-x}Ti_x$, and not pure Al after the reduction reaction during ball milling or due to decomposition of $NaAlH_4$. A high resolution image of a typical surface $Al_{1-x}Ti_x$ crystallite is shown in Fig. 5. Lattice fringes, corresponding to (1 1 1) planes, are visible in the image and they extend out to the surface. Defects, such as edge dislocations, may be of vital importance for the superior kinetics demonstrated for Ti enhanced $NaAlH_4$. The high resolution image in Fig. 5b is a filtered image constructed purely by the elastic, Bragg scattered intensity (right inset in Fig. 5a) in the Fourier transform image (left inset in Fig. 5a). The inelastic scattering is filtered out in the real space inverse Fourier transform image to better visualize lattice and dislocations. Only line defects along one of the four individual ⟨1 1 1⟩ directions are visible in each projection.

The solid line X-ray energy dispersive spectrum in Fig. 5c verifies that the surface crystallite is $Al_{1-x}Ti_x$, and not pure Al. A dotted line spectrum, acquired from a larger area representing more the average composition of the sample, is included for comparison. The Cu peak in the spectrum is due to the Cu grid and the environment around the sample and detector. Likewise, the C peak is due to the holey carbon film onto which the sample is dispersed. Further, it is notable that the O peaks in the two spectra are negligible. Measurements give an Al to Ti ratio corresponding to $Al_{0.83}Ti_{0.17}$. However, the k-factor in the Cliff–Lorimer equation [51] was not determined experimentally, and the thickness of the $Al_{1-x}Ti_x$ crystal was only

estimated. The value of x, given by the EDS software, should therefore be treated semi-quantitative rather than quantitative. Several spectra were acquired from different $Al_{1-x}Ti_x$ surface crystals. The value of x varied from 0.13 to 0.18. It is uncertain if these variations are real or partly due to different analyzed thicknesses. In addition, possible amorphous material, having a different composition than the crystalline $Al_{1-x}Ti_x$, might contribute to some of the spectra. Finally, a slightly inaccurate k-factor would introduce a systematic error in the measured Al to Ti ratio. However, an approximate value of 0.15 seems to be quite a reliable value, and is in excellent agreement with the $Al_{0.85}Ti_{0.15}$ composition determined by high resolution X-ray synchrotron data [42].

The high resolution image in Fig. 6a is from the surface of a $NaAlH_4$ crystal in a ball milled and twice H cycled $NaAlH_4 + 0.1FeCl_3$ sample. The bulk $NaAlH_4$ had decomposed before the image was acquired, but the outermost layer is unaffected by the electron beam. This layer, with a thickness ranging up to 20 nm, displays mainly amorphous contrast in high resolution, but has a few, distributed crystalline particles embedded in the layer. A crystalline particle is shown about 8 nm from the surface in Fig. 6a. The accompanying diffraction pattern (Fig. 6b) has a strong primary amorphous halo located between the Al(1 1 1) and (2 0 0) Bragg diffraction spots, confirming that the layer is not a crystal oriented away from Bragg condition. EDS analyses from the amorphous and crystalline parts of Fig. 6a are shown in Fig. 6c. The composition of the amorphous region (solid line) was found to be $Al_{0.67}Fe_{0.33}$, and $Al_{0.85}Fe_{0.15}$ was the measured composition when the beam was centered onto the crystal (dotted line). Again, these compositions should be treated semi-quantitative rather than exact. Since most of the Fe is bound as amorphous $Al_{1-x}Fe_x$, it is likely that the crystalline part is pure Al due to decomposition of $NaAlH_4$ rather than an $Al_{1-x}Fe_x$ solid solution crystal. Having the crystal surrounded by amorphous $Al_{0.67}Fe_{0.33}$, the EDS signal will be a combination of contributions from the amorphous and the crystalline phases. EDS analysis can then give an Al to Fe ratio of 85:15 even though the crystal is pure Al. However, based on EDS, one cannot exclude that the crystal contains some Fe. Small variations in the 2:1 Al to Fe ratio were found when EDS was done on other amorphous parts in the sample.

4. Conclusions

$NaAlH_4$ is extremely sensitive to oxidation and all sample handling must be performed inside a dry Ar atmosphere having O_2 and H_2O contents of less than 1 ppm. TEM investigations of oxidized samples can lead to incorrect conclusions about sample chemistry and structure. $NaAlH_4$ is highly unstable under the electron beam, and only techniques that can be performed with a low electron flux can be used to avoid sample decomposition. Such techniques include bright and dark field imaging at low magnification and selected area diffraction. EDS can also be performed to some degree. The $NaAlH_4$ decomposition sequence under the electron beam is different from the normal two step decomposition giving Na_3AlH_6 and NaH after the first and second decomposition, respectively. While some Na_3AlH_6 is observed, Na is lost directly from the $NaAlH_4$ under the electron beam. *In situ* observations of the nucleation and diffusion processes involved in the two decompositions given in Eqs. (1) and (2) are therefore impossible with TEM.

Low magnification TEM in combination with synchrotron X-ray diffraction can still be used to determine the location of all of the $Al_{1-x}TM_x$ phases in the sample. Even though $NaAlH_4$ decomposes under the electron beam, all TM containing phases are stable and can be investigated with atomic resolution. Composition, and both crystal and defect structure of the $Al_{1-x}TM_x$ phases can be determined by a combination of high resolution imaging, electron diffraction and EDS or EELS. The interface between the alanate and the different $Al_{1-x}TM_x$ phases is clearly important in TM enhanced alanate systems, but cannot be investigated by TEM due to the rapid decomposition of $NaAlH_4$.

Acknowledgments

Financial support from the Research Council of Norway (Synchrotron program) and from Nordic Energy Research is acknowledged.

References

[1] L. Schlapbach, A. Züttel, Nature 414 (2001) 353–358.
[2] B. Bogdanovic, M. Schwickardi, J. Alloys Compd. 253–254 (1997) 1–9.
[3] K.J. Gross, G.J. Thomas, C.M. Jensen, J. Alloys Compd. 330–332 (2002) 683–690.
[4] B. Bogdanovic, M. Felderhoff, M. Germann, M. Härtel, A. Pommerin, F. Schüth, C. Weidenthaler, B. Zibrowius, J. Alloys Compd. 350 (2003) 246–255.
[5] H.W. Brinks, C.M. Jensen, S.S. Srinivasan, B.C. Hauback, D. Blanchard, K. Murphy, J. Alloys Compd. 376 (2004) 215–221.
[6] C. Weidenthaler, A. Pommerin, M. Felderhoff, B. Bodanovic, F. Schüth, Phys. Chem. Chem. Phys. 5 (2003) 5149–5153.
[7] S. Singh, S.W.H. Eijt, J. Huot, W.A. Kockelmann, M. Wagemaker, F.M. Mulder, Acta Mater. 55 (2007) 5549–5557.
[8] S. Gomes, G. Renaudin, H. Hagemann, K. Yvon, M.P. Sulic, C.M. Jensen, J. Alloys Compd. 390 (2005) 305–313.
[9] R. Cantelli, O. Palumbo, A. Paolone, C.M. Jensen, M.T. Kuba, R. Ayabe, J. Alloys Compd. 446–447 (2007) 260–263.
[10] C. Rongeat, I. Llamas-Jansa, S. Doppiu, S. Deladda, A. Borgschulte, L. Schultz, O. Gutfleisch, J. Phys. Chem. B 111 (2007) 13301–13306.
[11] M. Resan, M.D. Hampton, J.K. Lomness, D.K. Slattery, Int. J. Hydrogen Energy 30 (2005) 1413–1416.
[12] M.T. Kuba, S.S. Eaton, C. Morales, C.M. Jensen, J. Mater. Res. 20 (2005) 3265–3269.
[13] A. Léon, G. Yalovega, A. Soldatov, M. Fichtner, J. Phys. Chem. C 112 (2008) 12545–12549.
[14] C.P. Baldé, H.A. Stil, A.M.J. van der Eerden, K.P. de Jong, J.H. Bitter, J. Phys. Chem. C 111 (2007) 2797–2802.
[15] J. Graetz, J.J. Reilly, J. Johnsen, A.Y. Ignatov, T.A. Tyson, Appl. Phys. Lett. 85 (2004) 500–502.
[16] A. Leon, O. Kircher, M. Fichtner, J. Rothe, D. Schild, J. Phys. Chem. B 110 (2006) 1192–1200.
[17] C. Rongeat, I.L. Jansa, S. Oswald, L. Schultz, O. Gutfleisch, Acta Mater. 57 (2009) 5563–5570.
[18] X.-D. Kang, P. Wang, H.-M. Cheng, J. Phys. Chem. C 111 (2007) 4879–4884.
[19] J. Iniguez, T. Yildirim, T.J. Udovic, M.P. Sulic, C.M. Jensen, Phys. Rev. B 70 (2004) 060101.
[20] Q. Shi, J. Voss, H.S. Jacobsen, K. Lefmann, M. Zamponi, T. Vegge, J. Alloys Compd. 446–447 (2007) 469–473.
[21] G. Majer, E. Stanik, L.E. Valiente Banuet, F. Grinberg, O. Kircher, M. Fichtner, J. Alloys Compd. 404–406 (2005) 738–742.
[22] M.H.W. Verkuijlen, P.J.M. van Bentum, E.R.H. van Eck, W. Lohstroh, M. Fichtner, A.P.M. Kentgens, J. Phys. Chem. C 113 (2009) 15467–15472.
[23] R. Kadono, K. Shimomura, K.H. Satoh, S. Takeshita, A. Koda, K. Nishiyama, E. Akiba, R.M. Ayabe, M. Kuba, C.M. Jensen, Phys. Rev. Lett. 100 (2008) 026401.
[24] A. Leon, O. Kircher, H. Rosner, B. Decamps, E. Leroy, M. Fichtner, A. Percheron-Guegan, J. Alloys Compd. 414 (2006) 190–203.
[25] C.M. Andrei, J. Walmsley, H.W. Brinks, R. Holmestad, S.S. Srinivasan, C.M. Jensen, B.C. Hauback, Appl. Phys. A 80 (2005) 709–715.
[26] M. Felderhoff, K. Klementiev, W. Grünert, B. Spliethoff, B. Tesche, J.M. Bellosta von Colbe, B. Bogdanovic, M. Härtel, A. Pommerin, F. Schüth, C. Weidenthaler, Phys. Chem. Chem. Phys. 6 (2004) 4369–4374.
[27] X.-D. Kang, P. Wang, H.-M. Cheng, J Appl. Phys. 100 (2006) 034914.
[28] D.D. Graham, L.F. Culnane, M. Sulic, C.M. Jensen, I.M. Robertson, J. Alloys Compd. 446–447 (2007) 255–259.
[29] S. Isobe, H. Yao, Y. Wang, H. Kawasaki, N. Hashimoto, S. Ohnuki, Int. J. Hydrogen Energy 35 (2010) 7563–7567.
[30] A. Leon, D. Schild, M. Fichtner, J. Alloys Compd. 404–406 (2005) 766–770.
[31] O.M. Løvvik, S.M. Opalka, Appl. Phys. Lett. 88 (2006) 161917.
[32] O.M. Løvvik, S.M. Opalka, Phys. Rev. B 71 (2005) 054103.
[33] J. Iniguez, T. Yildirim, Appl. Phys. Lett. 86 (2005) 103109.
[34] C.M. Araujo, R. Ahuja, J.M. Osorio Guillen, P. Jena, Appl Phys. Lett. 86 (2005) 251913.
[35] C.M. Araujo, S. Li, R. Ahuja, P. Jena, Phys. Rev. B 72 (2005) 165101.
[36] K. Bai, P.S.E. Yeo, P. Wu, Chem. Mater. 20 (2008) 7539–7544.
[37] S. Singh, S.W.H. Eijt, Phys. Rev. B 78 (2008) 224110.
[38] Z. Lodziana, A. Züttel, J. Alloys Compd. 471 (2009) L29–L31.
[39] A. Leon, O. Kircher, J. Rothe, M. Fichtner, J. Phys. Chem. B 108 (2004) 16372–16376.
[40] H.W. Brinks, B.C. Hauback, S.S. Srinivasan, C.M. Jensen, J. Phys. Chem. B 109 (2005) 15780–15785.
[41] A.G. Haiduc, H.A. Stil, M. Schwarz, P. Paulus, J.J.C. Geerlings, J. Alloys Compd. 393 (2005) 252–263.

[42] M.P. Pitt, P.E. Vullum, M.H. Sørby, M.P. Sulic, C.M. Jensen, J.C. Walmsley, R. Holmestad, B.C. Hauback, Acta Mater. 56 (2008) 4691–4701.
[43] G.-J. Lee, J.-H. Shim, Y.W. Cho, K.S. Lee, Int. J. Hydrogen Energy 33 (2008) 3748–3753.
[44] J.W. Kim, J.-H. Shim, S.C. Kim, A. Remhof, A. Borgschulte, O. Friedrichs, R. Gremaud, F. Pendolino, A. Züttel, Y.W. Cho, K.H. Oh, J. Power Sources 192 (2009) 582–587.
[45] X. Fan, X. Xiao, J. Hou, Z. Zhang, Y. Liu, Z. Wu, C. Chen, Q. Wang, L. Chen, J. Mater. Sci. 44 (2009) 4700–4704.
[46] J.L. Làbàr, Ultramicroscopy 103 (2005) 237–249.
[47] E. Rönnebro, D. Noréus, K. Kadir, A. Reiser, B. Bodganovic, J. Alloys Compd. 299 (2000) 101–106.
[48] H.J. Herley, W. Jones, Mater. Lett. 1 (1983) 131–136.
[49] C.M. Andrei, J. Walmsley, H.W. Brinks, D. Blanchard, B.C. Hauback, G.A. Botton, R. Holmestad, J. Phys. Chem. B 109 (2005) 4350–4356.
[50] H. Kimura, K. Sasamori, A. Inoue, Mater. Trans. JIM 39 (1998) 773–777.
[51] D.B. Williams, C.B. Carter, Transmission Electron Microscopy, vol. IV, Plenum Press, New York, 1996 (Chapter 35).